

ARTICLE

Received 14 Jan 2015 | Accepted 21 May 2015 | Published 1 Jul 2015

DOI: 10.1038/ncomms8596

OPEN

# Self-assembled 2D WSe<sub>2</sub> thin films for photoelectrochemical hydrogen production

Xiaoyun Yu<sup>1,\*</sup>, Mathieu S. Prévot<sup>1,\*</sup>, Néstor Guijarro<sup>1</sup> & Kevin Sivula<sup>1</sup>

WSe<sub>2</sub>—a layered semiconductor that can be exfoliated into atomically thin two-dimensional sheets—offers promising characteristics for application in solar energy conversion. However, the lack of controllable, cost-effective methods to scalably fabricate homogeneous thin films currently limits practical application. Here we present a technique to prepare controlled thin films of 2D WSe<sub>2</sub> from dispersions of solvent-exfoliated few-layer flakes. Flake self-assembly at a liquid/liquid interface (formed exceptionally from two non-solvents for WSe<sub>2</sub>) followed by substrate transfer affords large-area thin films with superior 2D flake alignment compared with traditional (liquid/air) self-assembly techniques. We further demonstrate, for the first time, solar-to-hydrogen conversion from solution-processed WSe<sub>2</sub> thin films. Bare photoelectrodes with a thickness of *ca.* 25 nm exhibit sustained p-type photocurrent under simulated solar illumination, and up to 1.0 mA cm<sup>-2</sup> at 0 V versus reversible hydrogen electrode with an added water reduction catalyst (Pt). The importance of the self-assembled morphology is established by photoelectrochemical and conductivity measurements.

<sup>1</sup>Laboratory for Molecular Engineering of Optoelectronic Nanomaterials, Institute of Chemical Sciences and Engineering, École Polytechnique Fédérale de Lausanne (EPFL), Station 6, CH H4 565, Lausanne 1015, Switzerland. \* These authors contributed equally to this work. Correspondence and requests for materials should be addressed to K.S. (email: kevin.sivula@epfl.ch).

Transition metal dichalcogenides (TMDs) with a layered crystal structure have recently gained extensive attention due to their ability to be exfoliated into atomically thin two-dimensional (2D) sheets. The unique mechanical, physical and chemical properties of these 2D TMDs have established them as promising candidates for high-performance flexible electronic and optoelectronic devices<sup>1</sup>. In particular, the semiconducting MoX<sub>2</sub> or WX<sub>2</sub> (X=S or Se) show tunable band-gap characteristics corresponding to the number of atomic layers<sup>2</sup>, and strong light-matter interactions that afford up to 10% absorption of incident solar illumination in a thickness of <1 nm—capturing sunlight stronger than common semiconductors (that is, GaAs and Si) by an order of magnitude<sup>3,4</sup>. Moreover, early studies on bulk (non-exfoliated) TMDs for solar energy conversion achieved impressive results. Notably, WSe<sub>2</sub>-based Schottky junctions achieved 8.6 (ref. 5) and 14% (ref. 6) energy conversion efficiency, respectively, in photovoltaic (PV) and photoelectrochemical (PEC) devices. Accordingly, outstanding performance in solar energy conversion with 2D TMD materials has been greatly anticipated.

To take advantage of the 2D nature of TMDs in solar applications, the well-known mechanical exfoliation technique (that is, the scotch tape method) has been recently employed. Micrometre-sized van der Waals p–n heterojunction devices have been constructed by few-layer MoS<sub>2</sub> and WSe<sub>2</sub>, and have been observed to be photoactive<sup>7,8</sup>. However, the further development of solar energy conversion devices using these materials, and their ultimate practical application, is hindered by the lack of a controllable method to fabricate large-area and continuous thin films with controllable layer orientation and suitable contact to a conducting substrate. While physical or chemical vapour deposition techniques can offer good control over thin-film preparation<sup>9,10</sup>, these methods require high temperatures and vacuum, which are less suitable for the economical production of large-area solar energy conversion devices. Solution-based processing methods, in contrast, offer a viable route. Indeed, the chemical exfoliation of TMDs (using lithium intercalation) can afford stable dispersions of 2D flakes suitable for controllable film formation<sup>11</sup>. However the concurrent change from the semiconducting 2H-phase to the metallic 1T-phase during chemical exfoliation causes a loss in photo-activity<sup>12,13</sup>. Alternatively solvent-assisted exfoliation<sup>14–16</sup> can yield semiconducting 2D flakes, though due to the defect-free flake surfaces produced, obtaining stable dispersions at high concentration and processing them into uniform thin films without layer restacking remain significant challenges. We recently reported a sonopolymer-assisted exfoliation method that, together with alkyl-trichlorosilane surfactants, gave extremely stable dispersions of high-concentration 2D MoS<sub>2</sub> in 1,2-dichlorobenzene (DCB), and showed promise for thin-film formation<sup>17</sup>. Nevertheless, the development of deposition methods that can offer precise control over film thickness and morphology from TMD dispersions remains essential for further implementation into solar energy conversion devices.

Here we present a novel method for the controlled processing of 2D WSe<sub>2</sub> dispersions into uniform large-area thin films with flakes oriented either edge-to-edge (parallel to the substrate) or in overlapping-aggregated morphologies. We leverage this method to demonstrate, for the first time, solar-to-hydrogen energy conversion from solution-processed WSe<sub>2</sub> thin films, and further gain insight into the importance of the film morphology on the photoelectrode performance.

## Results

**Flake exfoliation self-assembly and film deposition.** Generally in solution-based nanoparticle thin-film formation, precipitation

and aggregation lead to poor uniformity and inadequate contact with the substrate. While partial control over these aspects can be achieved using appropriate surfactants or nanoparticle surface ligands, conventional solution-based coating techniques (drop casting, spin coating or dip coating) still typically give rise to agglomerated structures after solvent evaporation, especially for 2D materials<sup>18</sup>. As such, much work has focused on applying the 2D template of a fluid/fluid interface for the assembly of nanomaterials, followed by transfer to a solid substrate to achieve thin-film formation in a controlled manner. The self-assembly of nanoparticles at a liquid/air interface—the so-called Langmuir–Blodgett technique—is the prototypical example of this approach<sup>19,20</sup>, and employing a liquid/liquid interface is a promising extension suitable for large-aspect ratio 2D materials<sup>18</sup>. Typically in liquid/liquid self-assembly techniques, nanoparticles dispersed in a hydrophilic phase are driven to a hydrophilic/hydrophobic interface using mechanical agitation or with an inducing agent<sup>18,21,22</sup>. For example in seminal work by Vanmaekelbergh and co-workers<sup>23</sup>, ethanol was used as an inducer for the self-assembly of gold nanoparticles at a water–heptane interface. Recently, Jia *et al.*<sup>24</sup> presented a similar approach with 2D sulphonated graphene by first dispersing the particles in the inducing solvent (ethanol) and injecting them into the water layer. However, solvent-exfoliated semiconducting TMD flake dispersions show poor stability in most solvents. Indeed, our attempts to apply traditional liquid/liquid self-assembly techniques were unsuccessful even with alkyl-trichlorosilane functionalized TMDs, as we observed aggregation during the flake migration and film organization processes rather than homogeneous film formation. Therefore, to enable the self-assembly of 2D TMDs we developed an approach to spatially confine the particles at the interface of two immiscible non-solvents for the TMD flakes, that is, ethylene glycol (EG), and hexane.

To demonstrate this deposition approach, we chose WSe<sub>2</sub> as a model TMD given its previously demonstrated performance as a non-exfoliated semiconductor in solar energy conversion devices. Accordingly, we began by extending our previously reported method for the sonopolymer-assisted exfoliation of MoS<sub>2</sub> to WSe<sub>2</sub>, demonstrating the generality of this approach<sup>17</sup>. Indeed a similar 2D sheet size (200–1,000 nm) and thickness (monolayer and few layer flakes) were obtained by exfoliating the bulk WSe<sub>2</sub> in DCB as described in the methods section.

To verify the exfoliation of the bulk WSe<sub>2</sub>, basic characterization was performed (Fig. 1). First, exfoliated material was compared with the bulk starting material by Raman spectroscopy (Fig. 1a). For the starting material, the peaks corresponding to the first order E<sub>2g</sub> and A<sub>1g</sub> Raman modes, respectively<sup>25</sup>, are clearly distinguished ~250 cm<sup>-1</sup> with a frequency difference of 4.0 cm<sup>-1</sup> (inset Fig. 1a). In contrast for the exfoliated sample, these modes are merged into one peak with a shoulder (frequency difference of 2.8 cm<sup>-1</sup>). This decrease in frequency difference, caused by the reduced influence of neighbouring layers, confirms the effective exfoliation of the WSe<sub>2</sub> into a 2D configuration<sup>26</sup>. Moreover, a weak Raman signal at 308 cm<sup>-1</sup> in the exfoliated material suggests that the product contains mostly few-layered WSe<sub>2</sub> (ref. 27), even though we observe the presence of some monolayer flakes by scanning electron microscopy (SEM). Importantly, no peak at 700 or 800 cm<sup>-1</sup> was observed, which would indicate a substantial formation of oxide<sup>28</sup>. To gain further insight in to the quality of the WSe<sub>2</sub>, W core level XPS spectra were analysed and the W peaks (Supplementary Fig. 1) match well with the bulk material<sup>29</sup>. The doublet peaks at 36 and 38 eV can be attributed to a small amount of W–O in exfoliated sample similar to other reports<sup>30</sup>. However, we note that the broad 5P<sub>3/2</sub> peak also is observed in the range of the oxide peaks and this was not considered in our fitting.

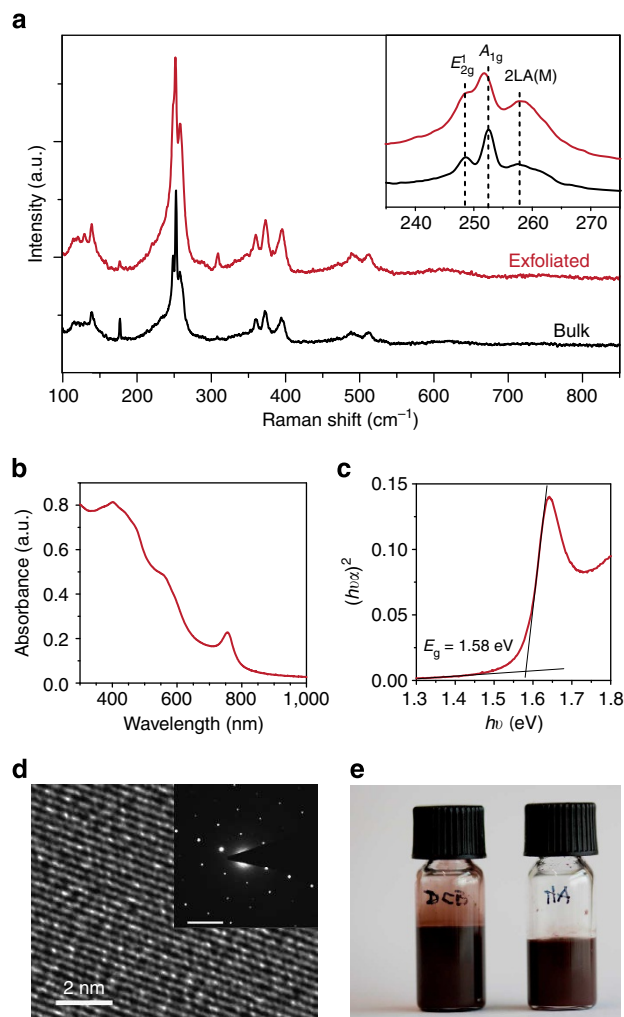


**Figure 1 | Basic characterization of the sonopolymer-assisted solvent-exfoliated WSe<sub>2</sub>.** (a) Survey and detailed (inset) Raman spectra of bulk WSe<sub>2</sub> and exfoliated WSe<sub>2</sub> after the washing process. (b) UV-vis absorption spectrum of WSe<sub>2</sub> dispersion in DCB and (c) the Tauc plot. (d) High-resolution-TEM image and SAED pattern (inset) of a single WSe<sub>2</sub> flake after solvent assisted exfoliation, scale bar in SAED, 5 nm<sup>-1</sup>. (e) A photograph of the WSe<sub>2</sub> dispersion in DCB solvent after 3 months (left) and WSe<sub>2</sub> dispersion after solvent exchange with hexylamine (right).

High-resolution TEM imaging of a single exfoliated WSe<sub>2</sub> flake (Fig. 1d) shows continuous lattice fringes demonstrating the single crystal nature of the exfoliated WSe<sub>2</sub>. This is supported by selective area electron diffraction (SAED, Fig. 1d inset), which shows the hexagonal crystal structure corresponding to the 2H phase of WSe<sub>2</sub>. The UV-vis spectrum of the exfoliated WSe<sub>2</sub> (Fig. 1b) shows several transition modes and an overall onset of *ca.* 800 nm. A direct band gap was estimated to be 1.58 eV by Tauc plot analysis (Fig. 1c), which is blue-shifted compared with the bulk material due to confinement effects<sup>31</sup>. The final dispersion of the exfoliated, hexyl-trichlorosilane (HTS) capped WSe<sub>2</sub> in DCB at high concentration (*ca.* 25 mg ml<sup>-1</sup>, Fig. 1e) was found to be stable for several months. We note that it was also possible to create stable dispersions of the WSe<sub>2</sub> in other solvents by adding the desired solvent after the washing procedure. Indeed, to transport the 2D WSe<sub>2</sub> flakes to the aforementioned EG/hexane liquid/liquid interface for self-assembly, the exfoliation solvent DCB is not suitable given its high density. Thus, hexylamine was selected as an alternative solvent due to its

intermediate density, miscibility with hexane and suitability to disperse the HTS functionalized 2D WSe<sub>2</sub> (at 10 mg ml<sup>-1</sup> a dispersion was found to be stable for hours).

Our space-confined self-assembled (SCSA) thin film deposition method proceeds as displayed in Fig. 2a. First, the WSe<sub>2</sub> dispersion is injected into the hexane layer near the EG/hexane interface. As the hexylamine rapidly dilutes into the hexane layer, the flakes become confined by the two non-solvents and quickly align with the 2D interface. Increasing the loading of flakes leads to in-plane self-compression and generates a compact 2D self-assembly of the TMD. Next, the hexane layer is removed from the top leaving the self-assembled thin-film floating on the surface of the EG. The EG can then be removed from the bottom (through fritted glass) affording the deposition of the SCSA WSe<sub>2</sub> film on a chosen substrate (for example, conductive F:SnO<sub>2</sub>-coated glass, SiO<sub>2</sub>/silicon or flexible Sn:In<sub>2</sub>O<sub>3</sub>-coated polyethylene terephthalate, PET, plastic). Finally, the film is dried at 150 °C to remove any residual EG and improve film adhesion.

Unlike conventional liquid/liquid interfacial self-assembly techniques, in which the solubility of the nanoparticles in one of the phases can allow folding and overlapping of the 2D structures, the two non-solvents employed in our approach provide much stronger confinement to the WSe<sub>2</sub> flakes at the interface. The effective use of the two non-solvents has been furthermore enabled by the high-concentration and stable TMD dispersion afforded by the exfoliation method and subsequent HTS functionalization. This allows only a small volume of the dispersion to be used maintaining the hexane phase a non-solvent. In addition for our approach, we note that overloading the flakes at the EG/hexane interface leads only to local small-area aggregates without affecting the entire film. This allows the facile and rapid preparation of large-area close-packed films of a single layer of flakes. Accordingly, the thickness of the SCSA film is insensitive to the processing conditions and determined by the flake thickness. Thicker films can be obtained by repeating the deposition process in a layer-by-layer strategy. A typical single flake layer SCSA film of WSe<sub>2</sub> on flexible Sn:In<sub>2</sub>O<sub>3</sub>-coated PET substrate is shown in Fig. 2b, and is homogeneous over a large area (7.5 cm<sup>2</sup>). Notably, this method is straightforward to scale up and homogeneous films up to 22.5 cm<sup>2</sup> have been prepared (see Supplementary Fig. 2). Transmission electron microscopy (TEM; Fig. 2c) provides further detail of the morphology of the horizontally oriented thin film. No significant aggregation or restacking of the flakes is observed due to the 2D alignment afforded by the SCSA film formation technique. We note that, due to the irregular shape of the solvent-exfoliated flakes, some spaces between flakes are present. Moreover, we can roughly estimate that the HTS remaining in the SCSA-deposited films is in the order of 10 mol% (that is, 1 HTS molecule for every 10 W atoms, see methods section).

To further illustrate the importance of the spatial confinement in the thin film formation process, we prepared WSe<sub>2</sub> thin films by injecting the hexylamine flake dispersion on the EG surface without a hexane top layer. As the hexylamine evaporates, we observe the partial restacking of the WSe<sub>2</sub> flakes indicated by a colour change and a relatively reduced lateral coverage of material on EG surface. After complete hexylamine removal, the aggregated WSe<sub>2</sub> film can be transferred to a substrate using the Langmuir-Blodgett technique, wherein the distance between WSe<sub>2</sub> aggregates is minimized by film compression. We note that the material consumption in this aggregated-compacted (AC) film formation approach is *ca.* 15 times higher than in the SCSA approach to obtain similar lateral surface coverage on the substrate. A video recording demonstrating the clear difference

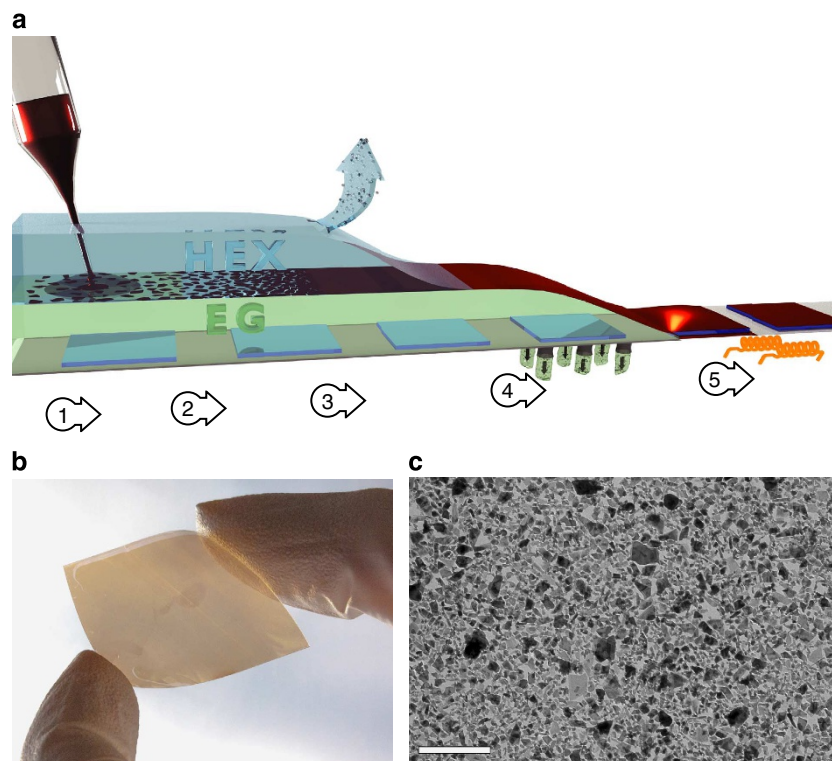


**Figure 2 | The space-confined self-assembly approach for 2D TMD thin-film deposition and results with WSe<sub>2</sub>.** (a) shows a schematic of the deposition method as described in the main text. Step 1: injection of WSe<sub>2</sub> dispersion; Step 2: flake confinement and self-assembly; Step 3: hexane removal; step 4: ethylene glycol removal and film deposition; step 5: drying at 150 °C. (b) displays a photograph of a single-flake-layer WSe<sub>2</sub> thin film deposited on flexible Sn:In<sub>2</sub>O<sub>3</sub> (ITO)-coated PET plastic, and (c) shows a representative TEM image of a single-flake-layer WSe<sub>2</sub> layer SCSA thin film deposited on a carbon-coated TEM grid. The scale bar is 2 μm.

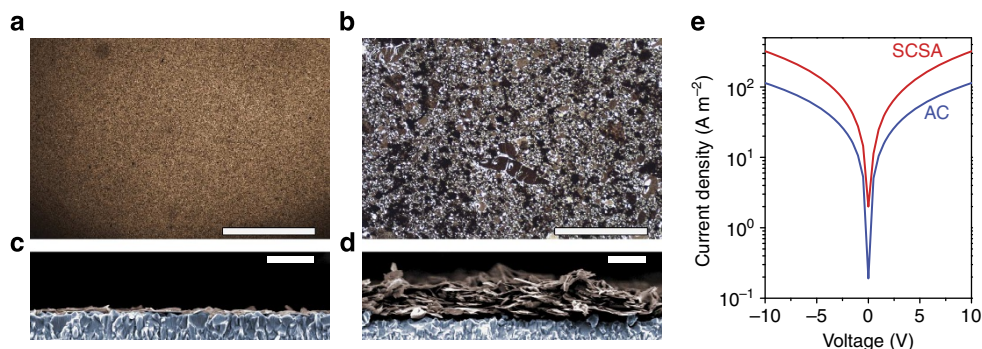


**Figure 3 | Morphological and electronic comparison of the SCSA and AC films.** (a,c) show diascopic optical microscopy and cross-sectional SEM images, respectively, for the SCSA film while (b,d) are for the AC film. Scale bars in (a,b), 500 μm; and scale bars in c,d, 400 nm. The SEM images are coloured to highlight the F:SnO<sub>2</sub> substrate (blue) and the WSe<sub>2</sub> (brown). (e) shows the *J*-*V* data for the conductivity measurement on the 20 μm channel device as described in the main text.

between the SCSA and AC assembly process at the 2D interface is included as Supplementary Movie 1.

**Morphological comparison and film conductivity.** The difference in morphology between the SCSA film and the AC film is shown with top-view (diascopic) optical microscopy and cross-sectional SEM images in Fig. 3. A homogeneous morphology is evident for the SCSA film on the millimetre length scale (Fig. 3a). Differences in the number of atomic layers in each flake and small spaces between the individual flakes do, however, give rise to some optical graininess on the 500 nm scale. In stark contrast, the

AC film (Fig. 3b) exhibits domains in the 10–100 μm range and large void spaces despite the compression of the film before deposition. While some areas of the AC film appear to have similar optical transmission as the SCSA film, other areas are considerably more opaque, suggesting a widely varying thickness of WSe<sub>2</sub> in this film. The cross-sectional images (Fig 3c,d) confirm that the film consists of a single flake layer and that flake orientation is parallel with the substrate in the case of the SCSA film, while much thicker films and more random flake orientation is observed in the AC film. We note that some roughness of the SCSA film is expected due to underlying substrate (F:SnO<sub>2</sub>-coated glass), and surprisingly despite regions of significant aggregation

in the AC film and overlapping flakes (see additional SEM images in Supplementary Fig. 3), much of the film is reasonably aligned with the substrate.

While the SCSA film deposition technique clearly affords significantly more homogeneous films with improved flake alignment compared with the liquid/air technique, the resulting edge-to-edge configuration potentially leads to poorer charge transport in the direction parallel to the substrate (compared with the AC film case where flake overlap can facilitate charge transport). To investigate this, two-electrode conductivity measurements over 20 or 60  $\mu\text{m}$  channels were performed on SCSA and AC films deposited on glass substrates. The resulting current density–voltage ( $J$ – $V$ ) curves (Fig. 3e and Supplementary Fig. 4) indicate that, despite the edge-to-edge configuration in the SCSA film, long range conductivity remains possible (corresponding to conductivity in the order of  $10^{-4} \text{ S m}^{-1}$ ). We note that the similar values found with 20 and 60  $\mu\text{m}$  channel lengths suggests the contact resistance between the gold electrodes and the  $\text{WSe}_2$  film can be considered negligible, see Supplementary Table 1. Remarkably, the AC film shows similar, but slightly lower, current density in the direction parallel to the substrate despite the film having an average thickness of 150 nm (as measured by profilometry), that is, more than 10 times the SCSA film. Indeed, a current density of an order of magnitude greater than that observed in the SCSA film would be expected in the AC film given its thickness, if the connectivity of the film was similar over the channel length. Thus the observed current density in the AC film implies that the charge transport is limited by the large void spaces between aggregates on the tens of micron length scale, which reasonably reduces the number of continuous charge carrier percolation pathways in the AC film. However, we cannot discount differences in conductivity caused by the increased requirement for carriers to hop between  $\text{WSe}_2$  layers in the AC film morphology. Indeed it is well-known that that carrier mobility in layered 2D TMDs is much higher in the lamellar plane compared with the out-of-plane direction<sup>32</sup>. In any case, the self-assembly afforded by our SCSA film formation technique is clearly beneficial for lateral charge transport over large distances.

However, while the gaps between the aggregates may limit horizontal conductivity in the AC film, we cannot discount the possibility that its aggregated morphology could provide advantages in specific applications where high surface-area semiconductor junctions are beneficial—for example, electro and PEC applications. Indeed, as illustrated by the SEM images, the aggregates in the AC films offer significantly increased surface roughness compared with the SCSA film, therefore a larger semiconductor–electrolyte junction and more efficient charge transfer could reasonably be expected<sup>33</sup>. Moreover, the observed morphology of the AC film, consisting of a certain number of vertically orientated flakes, may benefit charge transport towards the substrate, aided by the fast in-plane charge mobility in 2D  $\text{WSe}_2$ <sup>32</sup>. Thus while the SCSA and AC films give drastically different film morphologies resulting in disparate charge transport in the direction parallel to the substrate, it is not immediately clear which would be better suited for applications as large-area electrodes for energy conversion.

**PEC characterization.** To further examine the electronic behaviour of the  $\text{WSe}_2$  films, the PEC performance of the films deposited on conductive substrates were next assessed. In previous work, non-exfoliated (bulk)  $\text{WSe}_2$  was primarily investigated as an n-type photoanode for PEC oxidation reactions<sup>5,6</sup>. Indeed, its favourable light absorption and reported stability under oxidative conditions made it an attractive semiconductor for PEC

energy conversion using aqueous polyhalide-based redox systems<sup>34,35</sup>. More recently, Lewis and co-workers<sup>36</sup> reported PEC solar fuel production with p-type (Nb-doped)  $\text{WSe}_2$  bulk single crystals as photocathodes for hydrogen evolution via water reduction. While bare  $\text{WSe}_2$  electrodes exhibited negligible hydrogen production under illumination when polarized at potentials more positive than the reversible hydrogen electrode (RHE) reference potential, hydrogen evolution was observed from a catalyst (Pt/Ru)-coated  $\text{WSe}_2$  electrode in acidic electrolyte with a (1 sun) photocurrent density of  $24.5 \text{ mA cm}^{-2}$  at 0 V versus RHE. We examined our SCSA and AC electrodes (glass/F:SnO<sub>2</sub>/WSe<sub>2</sub>) under similar conditions and observed p-type behaviour without any intentional dopant added (consistent with undoped  $\text{WSe}_2$  measured by other techniques<sup>37,38</sup>). However, we cannot discount the HTS surfactant acting as a dopant<sup>39</sup>. The PEC performance is presented in Fig. 4. SCSA electrodes prepared from two layers were used to increase the light absorption for the PEC study. Despite an increased average thickness (25–30 nm for the two-layer case) the morphology was not different from the one-layer case (see Supplementary Fig. 5).

Linear scanning voltammetry (LSV) curves of the bare SCSA and AC electrodes were investigated under intermittent (chopped) illumination (1 sun,  $100 \text{ mW cm}^{-2}$ ) in 1 M  $\text{H}_2\text{SO}_4$  electrolyte are shown in Fig. 4a (top section). Here we note the onset of sustained p-type (cathodic) photocurrent at *ca.* +0.5 V versus RHE for both the SCSA and AC electrodes. The magnitude of the photocurrent was also similar for both—reaching a maximum of *ca.*  $40 \mu\text{A cm}^{-2}$  at 0 V versus RHE. We note that LSV measurements under chopped illumination show high dark currents due to transient effects. LSV measurements under constant dark or illumination conditions (Supplementary Fig. 6) confirm the dark current of the  $\text{WSe}_2$  films is similar to the bare F:SnO<sub>2</sub> substrate and also corroborate the photocurrent magnitude. The observation of sustained photocurrent is remarkable with the bare films considering the absence of photocurrent in the single crystal case under the same conditions<sup>36</sup>. It is likely that the reasonably high density of edge states in our films directly act as catalytic sites for the hydrogen evolution reaction (HER) as these edge sites have been shown to be catalytically active for the HER in analogous TMD materials<sup>40,41</sup>. Comparing the photon absorption and incident-photon-to-current (IPCE) spectra as a function of the illumination wavelength,  $\lambda$ , confirms that the observed cathodic photocurrent results from light absorption by the  $\text{WSe}_2$  (Fig. 4b). Indeed, the IPCE matches well with the absorption spectrum from the onset at  $\lambda = 800 \text{ nm}$  to about 550 nm where it then remains roughly constant until  $\lambda = 400 \text{ nm}$ . This leveling off of the IPCE along with the modest photocurrent compared with the amount of light absorbed by both the SCSA and AC films suggests that factors other than light absorption limit the photocurrent of the bare films.

We next deposited a Pt catalyst to facilitate the HER and to gain more insight into the limitations of the  $\text{WSe}_2$  electrodes. Surprisingly, we found significantly different behaviour between the SCSA and the AC films (Fig. 4a bottom section). While the magnitude of the sustained photocurrent was similar to the bare film in the AC case, large transient photocurrent spikes were observed on illumination, which quickly decayed to steady-state photocurrent in the  $50 \mu\text{A cm}^{-2}$  range. In contrast, the steady-state photocurrent of the SCSA electrode increased dramatically. The average photocurrent (out of eight replicate electrodes tested) at 0 V versus RHE for the Pt functionalized two-layer SCSA electrodes was  $0.78 \pm 0.17 \text{ mA cm}^{-2}$  and the highest measured was over  $1.0 \text{ mA cm}^{-2}$  (see Supplementary Fig. 7). To verify that the steady-state photocurrent was indeed due to hydrogen evolution in these electrodes, we measured  $\text{H}_2$  by

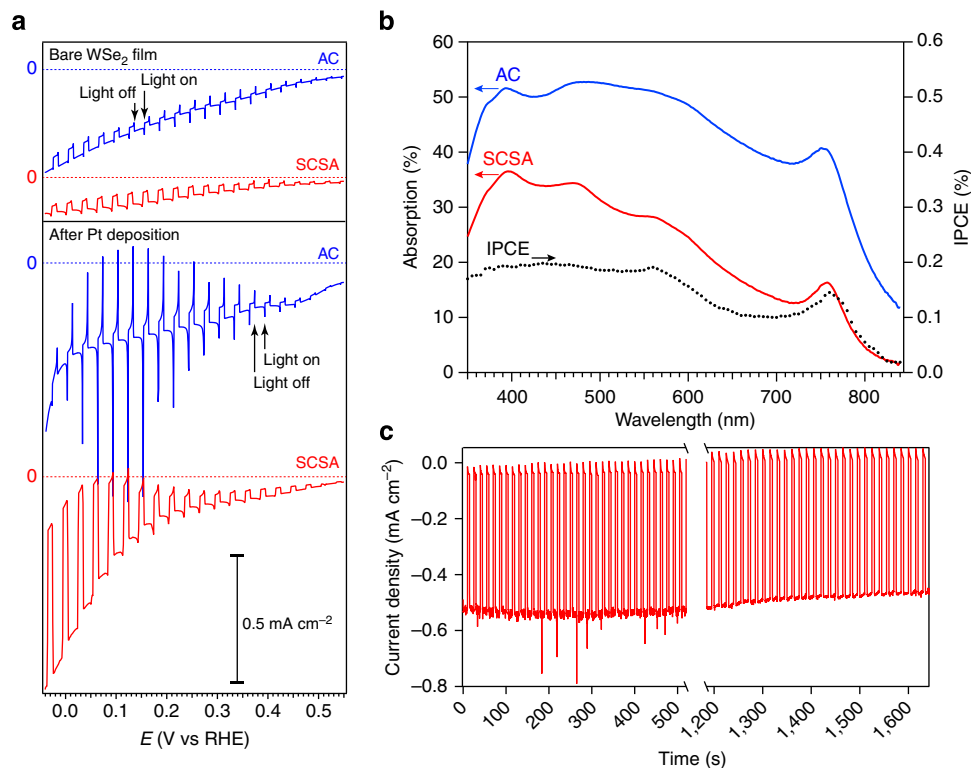


**Figure 4 | Photoelectrochemical characterization of the WSe<sub>2</sub> thin films prepared by the SCSA and AC techniques.** (a) shows the linear scanning voltammetry (LSV) curves under intermittent illumination (1 sun, 100 mW cm<sup>-2</sup>) for the bare films (top) and after Pt deposition (bottom). A horizontal axis corresponding to zero current is indicated for each curve. The incident-photon-to-current (IPCE) spectrum for the SCSA film is shown together with the optical absorptivity in b. (c) shows the chronoamperometric scan (at 0 V versus RHE) for the SCSA electrode under intermittent illumination.

gas chromatography (GC) under constant illumination and detected 103% of the hydrogen expected (compared with the photocurrent measured, See Supplementary Fig. 8), which is within the estimated 10% measurement error for a unity Faradaic efficiency of the HER on the SCSA electrodes. Moreover, similar to bulk single crystals, we observe good photoelectrode stability. Under constant polarization and intermittent illumination, insignificant change in the photocurrent was observed for tens of minutes (Fig. 4c). While longer stability measurements were not pursued in this work, the detachment of the Pt catalyst may decrease the photocurrent gradually. Despite this, the p-type WSe<sub>2</sub> itself has been shown to have a similar long-term stability as the n-type photoanodes<sup>36</sup>.

## Discussion

The greatly improved PEC performance of the Pt-functionalized SCSA electrode compared with the AC electrode is surprising given the increased light absorption and surface area for charge transfer from the semiconductor to the electrolyte in the AC film case, as suggested by the observed morphology. Given the different SCSA and AC film thicknesses, (25 nm and 150 nm, respectively, as measured by SEM and profilometry), one possible explanation for the observed difference is poor charge transport through the WSe<sub>2</sub> film in the AC film case. However, we eliminate this possibility by comparing the LSV curve for the AC electrode obtained from substrate-side illumination to the LSV from electrolyte-side illumination (See Supplementary Fig. 9). While the thickness of the AC film together with Beer–Lambert law indicates that 74% of the light absorption occurs in the first half of the film, equal performance was observed for both substrate-side and electrolyte-side illumination, suggesting

that photogenerated carriers produced in high proximity to the charge collecting substrate do not have an increased collection efficiency compared with charges generated far from the substrate. This observation and the presence of the aforementioned large photocurrent transients in the LSV of the AC film suggest that charge carrier accumulation is occurring at the semiconductor/substrate interface or the semiconductor/electrolyte interface. The similar catalyst deposition conditions used for both films further suggests the semiconductor/substrate interface as the limiting factor of the AC films. Indeed, we propose that the excellent 2D self-assembly enabled by the SCSA film deposition technique supports an improved semiconductor/substrate contact compared with the AC case, and thus enables the significantly improved steady-state solar-to-hydrogen conversion. We note that further characterization is required in order to more fully understand the differences in the film formation, flake connectivity and electronic interfaces on the nanometre length scale for both the of the deposition methods. These detailed studies are underway in our laboratories.

In a broader perspective, the *ca.* 1.0 mA cm<sup>-2</sup> hydrogen evolution photocurrent exhibited by the SCSA WSe<sub>2</sub> films in this work is much lower than the 24.5 mA cm<sup>-2</sup> obtained with optimized single crystal WSe<sub>2</sub> together with Ru/Pt catalyst<sup>36</sup>. However, the ability to easily prepare large-area substrates, and to absorb a significant fraction of the solar spectrum using films only ~10-nm thick are great advantages. Moreover our results, which clearly indicate the importance of HER catalysis and the semiconductor/substrate interface, offer points-of-interest to improve the performance of these solution-processed WSe<sub>2</sub> photocathodes for the ultimate integration in PEC tandem cells for high efficiency solar hydrogen production<sup>42</sup>. Further development of underlayers and catalysts for this system are

indeed underway in our laboratories. In addition, we suggest that the PEC study of solvent-exfoliated TMD materials, enabled by our material processing techniques, can be a valuable tool to aid the understanding and improvement of charge transport and transfer in these materials for application in PV and other optoelectronic devices. The extension of our methods to other TMDs and additional devices is also under development.

In summary, in this work we have presented for the first time, PEC water reduction from solution-processed WSe<sub>2</sub> thin-film electrodes. Remarkably, bare WSe<sub>2</sub> films showed measurable steady-state photocurrents without added catalyst. The further functionalization of these films with Pt gave hydrogen evolution photocurrents over 1.0 mA cm<sup>-2</sup> under standard illumination conditions. This demonstration was enabled by the development of a novel SCSA approach for solvent-exfoliated 2D WSe<sub>2</sub> flakes. The use of a liquid/liquid interface formed from two non-solvents for the WSe<sub>2</sub> enabled strong confinement and superior self-assembly compared with a traditional (liquid/air) interfacial self-assembly technique. We showed that the improved contact with the conducting substrate afforded by our self-assembly technique (compared with films prepared by a liquid/air self-assembly technique) directly leads to an improved steady-state solar-to-hydrogen conversion, and highlights the importance of film morphology on photoelectrode performance. Given that our SCSA deposition technique is suitable for the roll-to-roll fabrication of large-area thin films<sup>43</sup>, we expect that it will be useful in the facile preparation of thin film electrodes from other TMD and layered materials. Finally, given the initial results presented here with 2D WSe<sub>2</sub> and its promising aspects for solar fuel production, we anticipate future advances with this material deposited using solution-based self-assembly approaches.

## Methods

**Exfoliation of WSe<sub>2</sub>.** In a typical exfoliation of WSe<sub>2</sub>, commercially available powder (AlfaAesar, < 10 μm, 1.0 g) was dispersed in ca. 100 ml DCB. After sonication for 10 h in 0 °C bath (Qsonica Q700 probe sonicator, 50% amplitude, 5 s/1 s on/off cycles) large unexfoliated particles were removed by centrifugation (relative centrifugal force = 2,000g, 30 min). HTS (0.5 v/v %) was then added into the supernatant to avoid flake restacking. The sonopolymer, which is formed from the sonochemical decomposition of the DCB and has been shown to assist exfoliation, was removed from the dispersion by several washing cycles with chloroform as previously described<sup>17</sup>.

**Basic characterization.** To measure the concentration of WSe<sub>2</sub> in dispersion, 25 μl of the dispersion was dried in an aluminium pan, and weighted by Perkin Elmer AD 6 Autobalance. TEM, high-resolution-TEM and SAED were measured by FEI Tecnai Osiris electron microscope. SEM pictures were taken with a Zeiss Merlin microscope. The absorption spectra of the thin films were recorded by using a UV-vis-NIR UV-3600 (Shimadzu) spectrophotometer. Raman spectra were carried out on LabRAM HR Raman spectrometer with 532 nm Laser. W core XPS spectra were acquired with a KRATOS AXIS ULTRA spectrometer (Al Kα source, 600 × 750 μm spot size).

**SCSA and AC film deposition.** The thin film deposition was performed with HTS functionalized WSe<sub>2</sub> dispersion in hexylamine (ca. 10 mg ml<sup>-1</sup>) as described in the main text. Typically for the SCSA method, 20 μl of the WSe<sub>2</sub> dispersion was injected near an interface (area of 16 cm<sup>2</sup>) created from 15 ml of EG and 10 ml of hexane. After the 2D self-assembly, hexane was removed by a pipette and the film was allowed to dry. A low vacuum (~50 mbar) was used to assist removing EG from the bottom through fritted glass. A single SCSA deposition gave a thickness of ca. 10 nm (estimated by SEM), in correspondence with the quantity of WSe<sub>2</sub> injected (ca. 10 μg cm<sup>-2</sup>). For the AC film deposition, 300 μl of the WSe<sub>2</sub> dispersion was injected on to the EG in the absence of the hexane layer. The amount of the HTS capping agent remaining after the deposition was estimated in the following manner. Two separate one-flake-layer thin films of WSe<sub>2</sub> were deposited on glass substrates by the SCSA method from a non-HTS-modified WSe<sub>2</sub> dispersion (not a stable dispersion). After drying at 150 °C, one film was dipped in HTS solution (0.5 vol% in DCB solvent) for 30 min. Meanwhile the control film was dipped in neat DCB for the same time. Then the films were washed by DCB and hexane sequentially. The HTS coverage on the WSe<sub>2</sub> film was then estimated by XPS quantification based on the following two assumptions. (1) The post-HTS treatment modified only one side of the flakes. (2) The Si signal arising from the

substrate is constant since films are considered homogeneous over the area probed by the XPS (600 × 750 μm). We found the atomic ratio (Si/W) for the non-modified sample to be 1.10/1, while this ratio increases to 1.15/1 after HTS treatment. Accordingly, we can roughly estimate that the HTS remaining in the SCSA deposited films is in the order of 10 mol%.

**Conductivity measurements.** SCSA and AC films were deposited on bare glass, then two Au top electrodes were deposited using thermal resistance evaporation (Kurt J. Lesker Mini-SPECTROS) to construct a conductive channel (20 or 60 μm in length and 1 or 3 mm in width). The thickness of the SCSA and AC films in the channel were estimated to be ca. 10 nm (by SEM) and 150 nm (by profilometry), respectively. The *J-V* curves of WSe<sub>2</sub> films were measured in N<sub>2</sub> atmosphere in dark using a Keithley Model 2612 A Source Meter.

**PEC measurements.** SCSA and AC films were deposited on F:SnO<sub>2</sub>-coated glass substrate (Solaronix). The SCSA electrodes were made of two layers of the active material (thickness: 25–30 nm, see Supplementary Fig. 2). The electrodes were tested in a three-electrode set-up (BioLogic SP-200 potentiostat), with a Pt counter electrode and a Ag/AgCl KCl(sat) reference electrode. The electrolyte was a 1 M H<sub>2</sub>SO<sub>4</sub> solution in deionized water (pH 0) and the active area of the photoelectrode was 0.26 cm<sup>2</sup>. In a typical LSV acquisition, the voltage applied to the working electrode was swept cathodically (10 mV s<sup>-1</sup>) between 0.6 and 0 V versus RHE under intermittent illumination (simulated 1 sun with a filtered Xe arc lamp, illumination spectrum given in recent work<sup>44</sup>). Stability measurements were conducted by applying a constant voltage to the working electrode and recording the evolution of the photocurrent over time. The platinum electrocatalyst was deposited on the surface of the samples using the same three-electrode set-up with a 2 mM H<sub>2</sub>PtCl<sub>6</sub> aqueous deposition electrolyte. During the deposition, the sample was under illumination and the voltage was swept cathodically at 10 mV s<sup>-1</sup> between 0.6 and 0.1 V versus RHE and typically 5–6 mC of current was passed. After the deposition, the sample was rinsed with water and dried with compressed air.

**H<sub>2</sub> measurements and Faradaic efficiency calculation.** For this measurement, the working electrode was placed in a specifically designed, tightly closed PEC cell. The counter and reference electrodes, as well as the electrolyte, were the same as described in the PEC measurement section. A tube carrying Argon was inserted into the cell, with its output positioned to bubble the gas in the electrolyte. A second pipe was used to connect the cell headspace and a Clarus 480 Gas Chromatograph from Perkin Elmer. This allowed for real-time analysis of the composition of the gas produced inside the PEC cell. First, the electrolyte and small overhead space inside the cell were thoroughly purged with Argon (the purging process was monitored by GC analysis). Then the working electrode was set at +0.1 V versus RHE under illumination. After the photocurrent reached a steady-state value, the composition of the output gas flow was analysed by GC measurement. For a photocurrent of 9.39 μA (see Supplementary Fig. 8b), the GC spectrum gave an absolute H<sub>2</sub> signal of 0.1784. To estimate the Faradaic efficiency of the system, the H<sub>2</sub> detection system was calibrated using platinum foils as both the working and counter electrodes. For different values of steady state currents (obtained by setting the Pt working electrode at different potentials), the H<sub>2</sub> signal was measured by the GC. From these couple of values, a calibration curve was obtained (Supplementary Fig. 8a). Assuming Pt produces H<sub>2</sub> with 100% Faradaic efficiency, and based on the calibration thick curve, a 9.39 μA photocurrent should correspond to a GC signal of 0.1729. Since the signal we actually detected was 0.1784, the corresponding estimated Faradaic efficiency was 103%, with an estimated relative error of 10%.

## References

- Wang, Q. H., Kalantar-Zadeh, K., Kis, A., Coleman, J. N. & Strano, M. S. Electronics and optoelectronics of two-dimensional transition metal dichalcogenides. *Nat. Nanotech.* **7**, 699–712 (2012).
- Mak, K. F., Lee, C., Hone, J., Shan, J. & Heinz, T. F. Atomically thin MoS<sub>2</sub>: a new direct-gap semiconductor. *Phys. Rev. Lett.* **105**, 136805 (2010).
- Bernardi, M., Palumbo, M. & Grossman, J. C. Extraordinary sunlight absorption and one nanometer thick photovoltaics using two-dimensional monolayer materials. *Nano Lett.* **13**, 3664–3670 (2013).
- Britnell, L. *et al.* Strong light-matter interactions in heterostructures of atomically thin films. *Science* **340**, 1311–1314 (2013).
- Bourezg, R., Couturier, G., Salardenne, J., Doumerc, J. P. & Lévy, F. Interface of WSe<sub>2</sub> photoanodes in aqueous solution. II. photoelectrochemical properties. *Phys. Rev. B* **46**, 15411–15415 (1992).
- Tenne, R. & Wold, A. Passivation of recombination centers in n-WSe<sub>2</sub> yields high efficiency (14%) photoelectrochemical cell. *Appl. Phys. Lett.* **47**, 707–709 (1985).
- Lee, C.-H. *et al.* Atomically thin p-n junctions with van der Waals heterointerfaces. *Nat. Nanotech.* **9**, 676–681 (2014).
- Furchi, M. M., Pospischil, A., Libisch, F., Burgdorfer, J. & Mueller, T. Photovoltaic effect in an electrically tunable van der Waals heterojunction. *Nano Lett.* **14**, 4785–4791 (2014).

9. Liu, K.-K. *et al.* Growth of large-area and highly crystalline MoS<sub>2</sub> thin layers on insulating substrates. *Nano Lett.* **12**, 1538–1544 (2012).
10. Tarasov, A. *et al.* Highly uniform trilayer molybdenum disulfide for wafer-scale device fabrication. *Adv. Funct. Mater.* **24**, 6389–6400 (2014).
11. Zhiyuan, Z. *et al.* Single-layer semiconducting nanosheets: high-yield preparation and device fabrication. *Angew. Chem. Int. Ed.* **50**, 11093–11097 (2011).
12. Voiry, D. *et al.* Conducting MoS<sub>2</sub> nanosheets as catalysts for hydrogen evolution reaction. *Nano Lett.* **13**, 6222–6227 (2013).
13. Voiry, D. *et al.* Covalent functionalization of monolayered transition metal dichalcogenides by phase engineering. *Nat. Chem.* **7**, 45–49 (2015).
14. Cunningham, G. *et al.* Solvent exfoliation of transition metal dichalcogenides: dispersibility of exfoliated nanosheets varies only weakly between compounds. *ACS Nano* **6**, 3468–3480 (2012).
15. Nicolosi, V., Chhowalla, M., Kanatzidis, M. G., Strano, M. S. & Coleman, J. N. Liquid exfoliation of layered materials. *Science* **340**, 1420–1437 (2013).
16. Udayabagya, H. *et al.* A rational design of cosolvent exfoliation of layered materials by directly probing liquid–solid interaction. *Nat. Commun.* **4**, 2213–2219 (2013).
17. Yu, X., Prévot, M. S. & Sivula, K. Multiflake thin film electronic devices of solution processed 2D MoS<sub>2</sub> enabled by sonopolymer assisted exfoliation and surface modification. *Chem. Mater.* **26**, 5892–5899 (2014).
18. Biswas, S. & Drzal, L. T. A novel approach to create a highly ordered monolayer film of graphene nanosheets at the liquid–liquid interface. *Nano Lett.* **9**, 167–172 (2008).
19. Tachibana, H. *et al.* Electrical conductivity of hybrid Langmuir–Blodgett films of transition metal dichalcogenide and amphiphilic cations. *Synth. Met.* **102**, 1485–1486 (1999).
20. Tachibana, H., Yamanaka, Y., Sakai, H., Abe, M. & Matsumoto, M. Highly conductive inorganic–organic hybrid Langmuir–Blodgett films based on MoS<sub>2</sub>. *Chem. Mater.* **12**, 854–856 (2000).
21. Kim, F., Cote, L. J. & Huang, J. Graphene oxide: surface activity and two-dimensional assembly. *Adv. Mater.* **22**, 1954–1958 (2010).
22. Hu, L., Wu, L., Liao, M. & Fang, X. High-performance NiCo<sub>2</sub>O<sub>4</sub> nanofilm photodetectors fabricated by an interfacial self-assembly strategy. *Adv. Mater.* **23**, 1988–1992 (2011).
23. Reincke, F., Hickey, S. G., Kegel, W. K. & Vanmaekelbergh, D. Spontaneous assembly of a monolayer of charged gold nanocrystals at the water/oil interface. *Angew. Chem. Int. Ed.* **43**, 458–462 (2004).
24. Jia, B. *et al.* A new oil/water interfacial assembly of sulphonated graphene into ultrathin films. *RSC Adv.* **4**, 34566–34571 (2014).
25. del Corro, E. *et al.* Excited excitonic states in 1L, 2L, 3L, and bulk WSe<sub>2</sub> observed by resonant Raman spectroscopy. *ACS Nano* **8**, 9629–9635 (2014).
26. Li, H., Wu, J., Yin, Z. & Zhang, H. Preparation and applications of mechanically exfoliated single-layer and multilayer MoS<sub>2</sub> and WSe<sub>2</sub> nanosheets. *Acc. Chem. Res.* **47**, 1067–1075 (2014).
27. Zhao, W. *et al.* Lattice dynamics in mono- and few-layer sheets of WS<sub>2</sub> and WSe<sub>2</sub>. *Nanoscale* **5**, 9677–9683 (2013).
28. Li, H. *et al.* Mechanical exfoliation and characterization of single- and few-layer nanosheets of WSe<sub>2</sub>, TaS<sub>2</sub>, and TaSe<sub>2</sub>. *Small* **9**, 1974–1981 (2013).
29. Eng, A. Y., Ambrosi, A., Sofer, Z., Simek, P. & Pumera, M. Electrochemistry of transition metal dichalcogenides: strong dependence on the metal-to-chalcogen composition and exfoliation method. *ACS Nano* **8**, 12185–12198 (2014).
30. Wang, H. *et al.* MoSe<sub>2</sub> and WSe<sub>2</sub> nanofilms with vertically aligned molecular layers on curved and rough surfaces. *Nano Lett.* **13**, 3426–3433 (2013).
31. Ding, Y. *et al.* First principles study of structural, vibrational and electronic properties of graphene-like MX<sub>2</sub> (M = Mo, Nb, W, Ta; X = S, Se, Te) monolayers. *Phys. B* **406**, 2254–2260 (2011).
32. Jung, Y. *et al.* Metal seed layer thickness-induced transition from vertical to horizontal growth of MoS<sub>2</sub> and WS<sub>2</sub>. *Nano Lett.* **14**, 6842–6849 (2014).
33. Osterloh, F. E. Inorganic nanostructures for photoelectrochemical and photocatalytic water splitting. *Chem. Soc. Rev.* **42**, 2294–2320 (2013).
34. Kline, G., Kam, K. K., Ziegler, R. & Parkinson, B. A. Further studies of the photoelectrochemical properties of the group VI transition metal dichalcogenides. *Sol. Energ. Mater.* **6**, 337–350 (1982).
35. Simon, R. A., Ricco, A. J., Harrison, D. J. & Wrighton, M. S. Improvement of the photoelectrochemical oxidation of halides by platinization of metal dichalcogenide photoanodes. *J. Phys. Chem.* **87**, 4446–4453 (1983).
36. McKone, J. R., Pieterick, A. P., Gray, H. B. & Lewis, N. S. Hydrogen evolution from Pt/Ru-coated p-type WSe<sub>2</sub> photocathodes. *J. Am. Chem. Soc.* **135**, 223–231 (2012).
37. Fang, H. *et al.* High-performance single layered WSe<sub>2</sub> p-FETs with chemically doped contacts. *Nano Lett.* **12**, 3788–3792 (2012).
38. Abruna, H. D. & Bard, A. J. Semiconductor electrodes. 44. photoelectrochemistry at polycrystalline p-Type WSe<sub>2</sub> films. *J. Electrochem. Soc.* **129**, 673–675 (1982).
39. Kang, D.-H. *et al.* Controllable nondegenerate p-Type doping of tungsten diselenide by octadecyltrichlorosilane. *ACS Nano* **9**, 1099–1107 (2015).
40. Jaramillo, T. F. *et al.* Identification of active edge sites for electrochemical H<sub>2</sub> evolution from MoS<sub>2</sub> nanocatalysts. *Science* **317**, 100–102 (2007).
41. Bonde, J., Moses, P. G., Jaramillo, T. F., Nørskov, J. K. & Chorkendorff, I. Hydrogen evolution on nano-particulate transition metal sulfides. *Faraday Discuss.* **140**, 219–231 (2008).
42. Prévot, M. S. & Sivula, K. Photoelectrochemical tandem cells for solar water splitting. *J. Phys. Chem. C* **117**, 17879–17893 (2013).
43. Embs, F. W., Winter, H. H. & Wegner, G. Langmuir–Blodgett multilayer assembly by a continuous process using a steadily flowing subphase. *Langmuir* **9**, 1618–1621 (1993).
44. Prévot, M. S., Guijarro, N. & Sivula, K. Enhancing the performance of a robust sol-gel-processed p-type delafossite CuFeO<sub>2</sub> photocathode for solar water reduction. *Chem.Sus.Chem.* **8**, 1359–1367 (2015).

## Acknowledgements

The Swiss Competence Centers for Energy Research (SCCER Heat and Electricity Storage, contract # KTL.2014.0113) is acknowledged for financial support. We thank the Interdisciplinary Centre for Electron Microscopy (CIME) for assistance with electron microscopy, and the Earth and Planetary Science Laboratory (EPSL) for use of the Raman spectrometer. N.G. thanks the European Commission's Framework Project 7 for the financial support through a Marie-Curie Intra-European Fellowship (COCHALPEC, Project 326919).

## Author contributions

X.Y. developed the exfoliation and deposition techniques, prepared the thin films and performed the conductivity measurements. M.S.P. and X.Y. performed morphological characterization (optical and electron microscopy). M.S.P. performed the photoelectrochemical characterization. M.S.P. and N.G. performed the GC measurements for hydrogen gas detection. K.S., X.Y. and M.S.P. prepared the manuscript and subsequent editing/improvement was performed by all authors.

## Additional information

**Supplementary Information** accompanies this paper at <http://www.nature.com/naturecommunications>

**Competing financial interests:** The authors declare no competing financial interests.

**Reprints and permission** information is available online at <http://npg.nature.com/reprintsandpermissions/>

**How to cite this article:** Yu, X. *et al.* Self-assembled 2D WSe<sub>2</sub> Thin Films for Photoelectrochemical Hydrogen production. *Nat. Commun.* **6**:7596 doi: 10.1038/ncomms8596 (2015).



This work is licensed under a Creative Commons Attribution 4.0 International License. The images or other third party material in this article are included in the article's Creative Commons license, unless indicated otherwise in the credit line; if the material is not included under the Creative Commons license, users will need to obtain permission from the license holder to reproduce the material. To view a copy of this license, visit <http://creativecommons.org/licenses/by/4.0/>